Analysis of the influence of an interceptor on the transom flow of a fast ship by pressure reconstruction from stereoscopic scanning PIV

Jacobi, G.; Thill, C. H.; van 't Veer, Riaan; Huijsmans, R. H.M.

DOI
10.1016/j.oceaneng.2019.02.062

Publication date
2019

Document Version
Final published version

Published in
Ocean Engineering

Ocean Engineering 181 (2019) 281–292

Contents lists available at ScienceDirect

Ocean Engineering

journal homepage: www.elsevier.com/locate/oceaneng

Analysis of the influence of an interceptor on the transom flow of a fast ship by pressure reconstruction from stereoscopic scanning PIV

G. Jacobi*, C.H. Thill, R. van't Veer, R.H.M. Huijsmans

TU Delft, Department of Maritime and Transport Technology, Mekelweg 2, 2628CD, Delft, the Netherlands

ARTICLE INFO

Keywords:
Underwater PIV
Pressure reconstruction
PIV uncertainty
Interceptor

ABSTRACT

The present study describes the application of the particle image velocimetry (PIV) technique for the reconstruction of hydrodynamic pressures and loads on a ship model from measured velocity fields during towing tank tests. As an alternative to conventional pressure and force measurement techniques the method simultaneously pictures the velocity field and captures the dynamic aspect of the flow. The presented measurements are conducted in the transom region of a generic hull of a planing vessel which is equipped with an interceptor to create a stagnating flow, associated with a high pressure peak. The flow close to the hull is captured with an underwater stereoscopic PIV system and the pressure peak in front of the interceptor is reconstructed from time-averaged velocity fields. Results show the effect of different interceptor heights on the pressure distribution in the center-plane of the model. Further, a 3D flow field is reconstructed from scanning PIV measurements to analyze the lift reduction due to the finite span of the interceptor. The spatial variation of the measurement uncertainty is analyzed and propagated to the pressure field uncertainty and the potential of the method is further evaluated by comparison with numerical results from steady Reynolds Averaged Navier-Stokes (RANS) simulations.

1. Introduction

As soon a ship operates at high forward speeds its weight is predominantly supported by hydrodynamic, rather than hydrostatic forces. Small changes in the dynamic pressure distribution on the ship hull can have a significant influence on the ship's running attitude and performance. In order to further improve these vessels it is thus important to investigate the flow in the vicinity of the ship hull and to accurately determine global as well local pressure distributions.

While there has been steady development and improvement of numerical tools to analyze the flow physics and the ship's structural and motion response, towing tank experiments are needed for their experimental validation. However, traditional towing tank tests mainly focus on the assessment of global loads during captive model tests. The spatial resolution of such measurements can be improved by usage of segmented models where the ship is divided into several segments, which are connected to a rigid backbone via several force balances. As shown by Keuning (1994) and De Jong and Keuning (2006), who both performed towing tank tests with a high-speed craft model, consisting of 7 segments, these tests could give additional insights into the distribution of hydrodynamic forces over the length of the ship hull. By performing forced oscillation tests, added mass and damping coefficients of the segments were determined. However, local effects could not be captured. Whenever a more detailed picture of the pressure distribution has to be drawn, single pressure sensors can be fitted into the ship hull to measure pressures at discrete points. If accumulated to arrays even a discretized representation of the pressure distribution can be assessed. However, due to their size, resolution is limited and a change of the measurement position involves time intensive repositioning of the transducers. Furthermore, a flush installation into the faired hull is desired to minimize the disturbance of the local flow. An application for high-speed craft is reported by Choi (2018), where an array of 63 pressure sensors was used to determine a time averaged pressure distribution in the bow region of a fast displacement ship.

In aerodynamic applications, the usage of pressure sensitive paint (PSP) is a common means to accurately measure the pressure distribution on a surface with a high resolution (McLachlan and Bell, 1995). This cannot be considered as an option for towing tank application, where due the incompressibility of the fluid this technique can only detect the oxygen concentration (Sakaue et al., 2009), but not pressure. Another technique which has been increasingly applied in recent years for pressure measurement on surfaces, as well in the entire flow field, is the pressure reconstruction derived from particle image

* Corresponding author.
E-mail address: g.jacobi@tudelft.nl (G. Jacobi).

https://doi.org/10.1016/j.oceaneng.2019.02.062
Received 3 September 2018; Received in revised form 19 February 2019; Accepted 20 February 2019
Available online 16 April 2019
0029-8018/

velocimetry (PIV) measurements. As, to the knowledge of the author, in towing tank applications, the PIV technique has been so far only used to study the flow kinematics, in this paper its application for pressure reconstruction during towing tank tests will be investigated.

When applied to the measured velocity field from PIV measurements, the Navier-Stokes equations can be utilized to derive the pressure in the flow field and on the surface from the flow properties without any disturbance of the flow field in the measurement region. The recent development of the PIV technique and hardware components nowadays allows for a reconstruction of the 3D volumetric and even time resolved pressure fields using tomographic or stereoscopic scanning PIV. A detailed review of the main principles of PIV-based pressure measurement and a discussion of the methods' accuracy has been presented by Van Oudheusden (2013). Pressure reconstruction from PIV measurements is well studied and widely accepted in numerous aerodynamic and hydrodynamic applications. For aerodynamic applications the performance of pressure PIV and PSP measurements has been compared by Tagliabue et al. (2017). A good example of a practical application is given by Ragni et al. (2012) who used multiplane stereo PIV measurements to assess the loads of an aircraft propeller. In the field of ship hydrodynamics the technique has been successfully applied by Nila et al. (2013) to estimate slamming loads during the water entry of rigid bodies. For the case of hydrodynamic applications it has to be emphasized that due to the reconstruction of the pressure field from measured velocities, this method only measures the dynamic pressure component.

To investigate the possibilities of capturing the dynamic aspect of the flow around ships and loads on the ship hull, in the present study the pressure PIV technique will be applied to flow measurements in the direct vicinity of a ship model. The presented measurements are conducted in the transom region of a generic hull of a planing vessel with a flat bottom aft section. The transom of the model is equipped with an interceptor, which behaves comparable to a forward-facing step. When deployed at high speeds, the interceptor blade creates a stagnation region on the bottom of the hull in front of the transom, which is associated with a high pressure peak. Typical blade heights are in the order of magnitude of the boundary layer height. A schematic drawing of the interceptor and its influence on boundary layer flow and wall pressure distribution is depicted in Fig. 1. Mainly used in static configurations the generated lift is used to influence the trim of a ship. By dynamically changing the height of the interceptor it is also used for active ride-control of fast ships in waves.

The flow around interceptors and the resulting hydrodynamic forces are well studied with numerical methods by Brizzolara (2003) and Villa and Brizzolara (2009) with potential and RANSE methods. Molini and Brizzolara (2005) also discussed the 3d effects of an interceptor with a finite span. However, 3d results were obtained without taking the influence of the boundary layer into account. A more recent study has been undertaken by Pearce and Brandner (2014) who compared analytical and potential methods to predict the cavitating flow over a wall

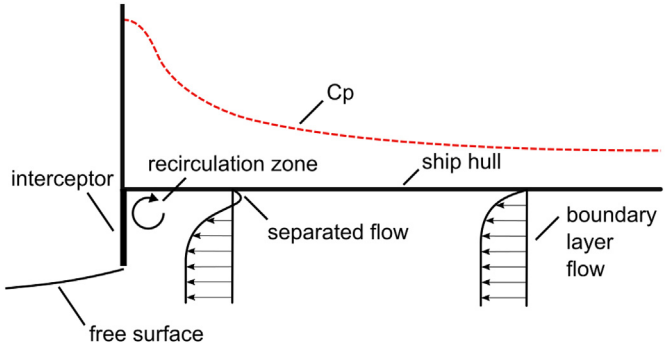

Fig. 1. Schematic drawing of the boundary layer flow and wall pressure distribution in front of an interceptor.

mounted fence. On the experimental side, segmented model tests have been performed by Rijkens et al. (2013) to investigate the hydrodynamic characteristics of different interceptor configurations. Mansoori and Fernandes (2015) performed a more fundamental analysis by experimentally and numerically analyzing the performance of an interceptor which was mounted to a flat plate.

The aim of this study is to correctly capture the flow close to the ship hull and reconstruct the pressure peak in front of the interceptor from time-averaged velocity fields. The spatial variation of uncertainty is analyzed and propagated to the pressure field uncertainty. The 2d pressure field in the center-plane of the model is reconstructed from planar stereo PIV measurements showing the effect of different interceptor heights. The three-dimensional effects of the flow on the pressure distribution in front of the interceptor are captured with stereoscopic scanning PIV measurements. Finally the potential of the pressure PIV method is further evaluated by comparing experimental with numerical results from steady Reynolds Averaged Navier-Stokes (RANS) simulations.

2. Experimental setup

The PIV experiments are performed at the large towing tank of the ship hydrodynamics laboratory at Delft University of Technology. The tank has a cross section of 4.22 m width and 2.5 m depth over a test section length of 142 m. The carriage is able to operate at a maximum speed of 7 m/s. A model of a generic planning hull with an overall length of 1.8 m is used in this study. The same model has already been used by Rijkens et al. (2013) to experimentally study the hydrodynamic performance of interceptors and transom flaps for the motion control of fast ships during segmented model tests. Its transom section has a simple box shape with a constant cross section being 0.4 m wide and 0.8 m long. To provide optical access to the measurement area for illumination with the laser sheet, the bottom of the segment is replaced by an acrylic glass plate. The bow segment is designed from developable surfaces with the purpose to smoothly divert the flow to the transom segment. At the transom of the model an interceptor of adjustable height is attached. Manufactured from a simple plate the interceptor covers the whole beam of the model. Four guiding rails guarantee a smooth and accurate setting of the interceptor intrusion height. To accurately position the model within the field of view of the PIV system and to set it to its correct running trim and sinkage, the model is mounted to the carriage via a Symmetrie NOTUS hexapod. With its linear travel range of ±250 mm it was also used to reposition the model in between runs during the scanning PIV tests and makes an extra traversing system for the PIV system obsolete. For all test runs the model is kept at a constant draft of 50 mm and constant bow-up trim of 3°, resulting in a wetted length of 1.52 m. For the 2d PIV measurements in the center-plane of the model, a test matrix with carriage speeds of 3, 4 and 5 m/s are performed, while the interceptor intrusion height is stepwise increased from 0 mm up to 20 mm with increments of 5 mm. The carriage speeds are equivalent to length based Froude numbers of 0.71, 0.95 and 1.19. Reynolds numbers, based on the wetted length of the ship, range from 5.4e4 to 9.0e5. A volumetric reconstruction from scanning PIV measurements is attempted for selected conditions at speeds of 3 and 4 m/s with interceptor heights of 10 and 20 mm. To capture the three-dimensionality of the flow field, the model position is shifted in the transverse direction between runs, resulting in a total number of 14 measurement positions from the center plane to the side of the model. As the three-dimensionality of the flow is expected to increase with increasing distance from the center plane, the spacing in between measurement planes is reduced from 20 mm in the center plane to 10 mm at the side of the model.

2.1. PIV setup

The flow in the vicinity of the interceptor is investigated with an

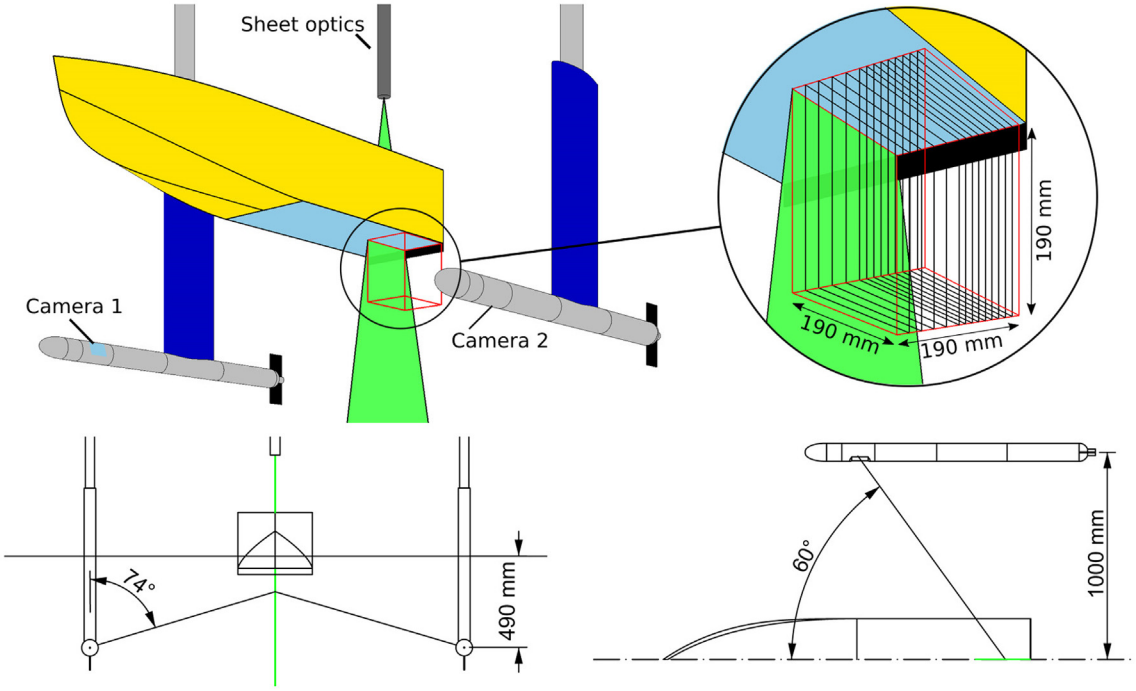

Fig. 2. Schematic drawing of the PIV setup.

underwater stereoscopic PIV setup. To minimize reflections from the bottom of the ship hull and increase the near wall resolution, the laser head and optics are placed above the water and the laser sheet is guided through the acrylic glass bottom of the model to the field of view. The two cameras are each located in a watertight torpedo-shaped housing. To get optical access to the region in front of the interceptor, the cameras are located approximately 680 mm in front of the transom, looking backwards to the field of view with a 60° mirror section. A symmetric arrangement with one camera on either side of the light sheet is used to accomplish a high accuracy determination of the out of plane velocity component. To prevent any disturbance of the flow in the measurement region, the struts which connect the torpedo to the carriage are positioned as far aft as the transom of the ship model and have a streamlined shape. The immersion depth of the torpedoes is 490 mm and their horizontal stand-off distance is 1000 mm. Fig. 2 shows a schematic drawing of the PIV setup indicating the position of the cameras and measurement planes.

For illumination of the measurement plane a Litron Bernoulli Nd:YAG laser with 200 mJ/pulse energy at a wave length of 532 nm is used. Image acquisition was done with two LaVision Imager Pro SX cameras with a sensor size of 2448 × 2050 pixels and 12 bit color depth. Equipped with lenses of 28 mm focal length, the field of view was approximately 200 × 200 mm^2. To keep the particles focused over the whole field of view, a Scheimpflug-adapter is mounted in front of each camera. With a pixel pitch of 3.45 μm, the digital resolution is approximately 10 pixels/mm. Images are recorded at a double frame acquisition rate of 7 Hz, resulting in 210 image pairs per measurement run at the lowest speed and 120 image pairs at the highest speed. Calibration of the cameras is done with a two-level double-sided 3d calibration plate which is carefully aligned in an iterative process with the moving direction of the carriage. Mounting the calibration plate to the hexapod enables for a highly accurate repositioning of the plate during the calibration process. To guarantee a uniform distribution of the 50 μm polymer (Vestosint) particles in the measurement area, a retractable seeding rake is mounted in front of the carriage. Prior to releasing the particles into the towing tank in between measurement runs, they are premixed in a high shear flow to prevent clustering. While after every measurement run the tank is reseeded, a waiting time of 25 min allows the water to settle in between runs.

3. PIV processing

As previously found by Jacobi et al. (2016), structural vibrations can occur at high towing velocities which significantly affect the quality of the image correlation. It was shown that vibrations of the measurement system, and thus the fluctuations of disparity increased at high carriage speeds. Based on the cross correlation of two images, taken at the same instant of time, Wieneke (2005) proposed a method to test for a static misalignment of the recombined stereo PIV images. Using the resulting disparity map, the initial calibration can be further refined, and calibration coefficients can be corrected for a static misalignment of the calibration plate. In most PIV applications conducted in a controlled laboratory environment this would be sufficient to completely correct for any misalignment of the laser sheet and the calibration plate. However, when the measurement system is prone to vibrations disparity will vary in time if cameras and light sheet optics are not rigidly connected. While the application of the self-calibration procedure proposed by Wieneke (2005) successfully removes the mean disparity in the recorded data set, a fluctuating disparity is left with an amplitude of approximately 10 pixels at the highest analyzed carriage speed of 5 m/s. To further reduce the amplitude of the fluctuating residual disparity a two-step correction procedure is introduced (Jacobi et al., 2016). In the first step, the disparity between all images for every single camera is reduced by correlating significant features of the ship hull. After an independent shift correction for both cameras, the image sets from both cameras still have a constant offset. This is corrected in a second step by performing a second self-calibration, using the mean disparity vector field of all recordings. The method significantly reduces the disparity over the whole tested speed range. However, the trend of increasing residual disparities with increasing carriage speed is still visible. While for carriage speeds of 1 m/s the root mean square of the fluctuating disparity could be reduced to 0.7 pixels, at 5 m/s the residual disparity was reduced to 2.5 pixels. Considering the recommendation that the displacement between particle pairs in dewarped images should not differ more than half the particle image size (2–3 pixels), this was found to be acceptable.

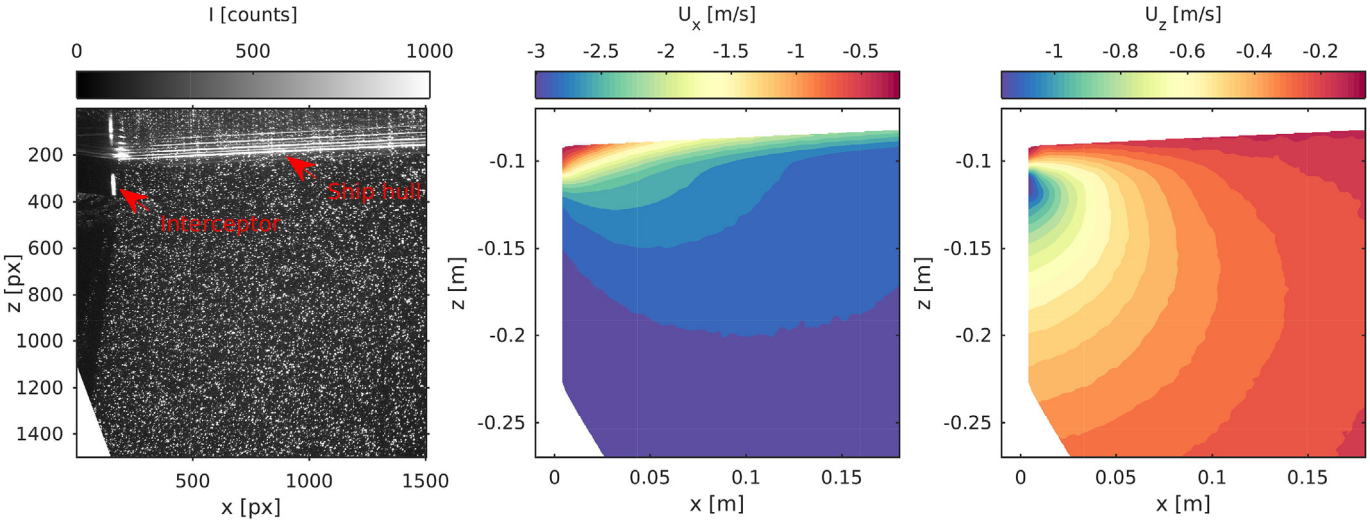

Fig. 3. Sample PIV image with reflections at hull bottom and interceptor (left); In plane velocity components from mean velocity field (right).

Data acquisition, as well as data post-processing is done using the commercial software package DaVis 8.4.0 from LaVision. Before finally calculating the velocity fields, a mask is applied to the images, to mask out reflections on the acrylic glass plate and to enhance correlation close to the ship hull and interceptor. The calculation of the velocity vector field is done in multiple correlation iterations. Starting with an interrogation window of 64 × 64 pixels in the initial pass, the window size is iteratively decreased to 24 × 24 pixels. The windows are overlapping by 50% and a Gaussian weighting function was used. Fig. 3 shows an example of a dewarped raw image and the in plane components from the mean velocity field which was obtained from 200 vector images. As seen from the velocity fields, the stagnation region in front of the interceptor is well captured, as well as the downward acceleration towards the tip of the interceptor. The coordinate system is chosen to match the ship coordinate system with the origin located at the transom of the model at 0° trim angle.

3.1. Pressure reconstruction and force determination

Having obtained the mean velocity field and its fluctuations from the statistical ensemble of the recorded velocity fields, one can describe the pressure gradient of the mean pressure field with Reynolds averaged momentum equation. The decomposition of the velocity into a time averaged and fluctuating part leads to:

$$\bar{u}_j \frac{\partial \bar{u}_i}{\partial x_j} = -\frac{1}{\rho}\frac{\partial \bar{p}}{\partial x_i} + \nu \frac{\partial^2 \bar{u}_i}{\partial x_j \partial x_j} - \frac{\partial \overline{u'_i u'_j}}{\partial x_j} \tag{1}$$

The pressure field can be either calculated from direct integration of the momentum equation or by solving the pressure Poisson equation, which is obtained by applying the divergence operator to the momentum equation:

$$\frac{\partial^2 \bar{p}}{\partial x_i^2} = \rho \frac{\partial}{\partial x_i}\left(-\bar{u}_j \frac{\partial \bar{u}_i}{\partial x_j} + \nu \frac{\partial^2 \bar{u}_i}{\partial x_j \partial x_j} - \frac{\partial \overline{u'_i u'_j}}{\partial x_j} \right) \tag{2}$$

Under the assumption that the flow is incompressible, the divergence free condition holds, i.e. $\nabla \cdot u = 0$. As a result the viscous term disappears and the pressure Poisson equation reduces to:

$$\frac{\partial^2 \bar{p}}{\partial x_i^2} = -\rho \frac{\partial}{\partial x_i}\left(\bar{u}_j \frac{\partial \bar{u}_i}{\partial x_j} + \frac{\partial \overline{u'_i u'_j}}{\partial x_j} \right) \tag{3}$$

The advantages and disadvantages of both methods have been extensively discussed by Van Oudheusden (2013). In this case the Poisson approach is chosen to reconstruct the pressure field, as it has been reported to produce less noisy results (Albrecht et al., 2012). The Reynolds stresses are found from variances and covariances of the velocity vectors. While in the symmetry plane of the ship model the flow is assumed to be two dimensional, all spatial derivatives, necessary for calculating the planar pressure field, are obtained from a single-plane measurement. For a calculation of the three dimensional pressure field in front of the interceptor, the spatial derivatives of the out-of-plane direction have to be obtained from the measured fields of adjacent measurement planes obtained from scanning PIV measurements along the transverse direction of the ship model.

For the solution of the Poisson equation a Neumann boundary condition is obtained from the Reynolds averaged momentum equation (1) to prescribe the non-homogeneous pressure gradient at the boundary of the measurement area:

$$n_i \cdot \frac{\partial \bar{p}}{\partial x_i} = -\rho n_i \cdot \left(\bar{u}_j \frac{\partial \bar{u}_i}{\partial x_j} - \nu \frac{\partial^2 \bar{u}_i}{\partial x_j \partial x_j} + \frac{\partial \overline{u'_i u'_j}}{\partial x_j} \right) \tag{4}$$

As only Neumann boundary conditions are used, a reference pressure is needed to correctly scale the reconstructed pressures. As no data from a reference pressure sensor is available, it is favorable to choose the reference pressure point to be in a region of undisturbed flow where it can be determined with the Bernoulli equation. However, due to the limited size of the measurement area, this was only possible for the smallest interceptor heights where the flow disturbance is small. To compare the reconstructed field with results from simulations a reference pressure is taken from the numerical results 180 mm in front of the transom and 180 mm below the ship bottom where the flow is disturbed the least. For the solution of the Poisson pressure equation, the OpenFOAM 5.0 package is employed where the equation is discretized with a finite volume method. Fig. 4 gives an example of the reconstructed pressure field in front of the interceptor and indicates the location P of the reference pressure point. The reconstructed pressure field shows an increase of the pressure coefficient towards the transom, with a clear pressure peak right in front of the interceptor in the stagnation region. As the maximum blade stroke is smaller than the boundary layer height and the flow is decelerated towards the wall in the boundary layer, the maximum pressure coefficient is well below 1.

The generated lift force from the interceptor will be obtained by numerically integrating the extrapolated pressure distribution over the length of the analyzed longitudinal segment of the model hull:

$$l = \left(\int \bar{p} \cdot \vec{n}\, dS \right) \cdot \vec{z} = \sum_{i=1}^{N} \overline{p_i} \cdot cos\theta ds_i \tag{5}$$

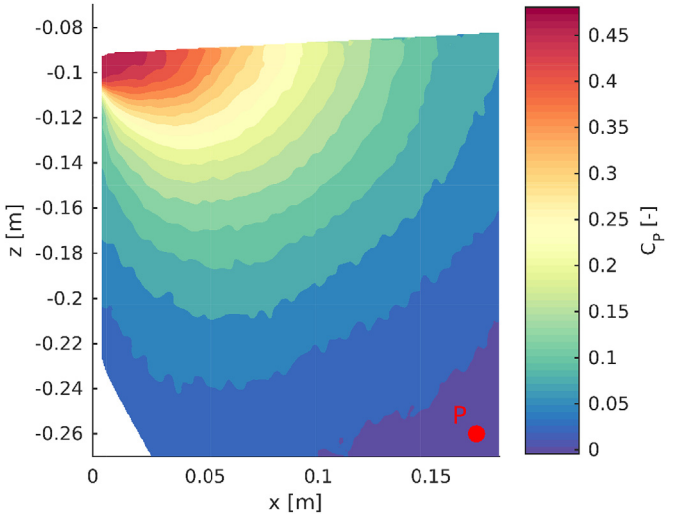

Fig. 4. Reconstructed pressure field with reference pressure point P at V_c = 3m/s with interceptor height h= 20 mm.

Here, $\vec{z}$ describes the direction normal to the freestream and θ is the trim angle of the ship model. With S being the length of the segment and V_c being the carriage velocity, the sectional lift coefficient per unit span is calculated as:

$$c_l = \frac{2l}{\rho V_c^2 S} \tag{6}$$

4. Measurement uncertainty assessment and propagation

4.1. Measurement uncertainty

As the quality of PIV measurements is influenced by multiple error sources it is challenging to consider all of these for a reliable estimation of velocity field uncertainty. However, a number of posteriori uncertainty estimation methods have been developed recently. Amongst these, the quantification of uncertainty based on the correlation statistics by Wieneke (2015) has shown to give a reliable estimate of the random uncertainty components. Looking only at the statistical quantities of the measured velocities, the uncertainty is, due to the finite sample size, typically dominated by random errors and justifies a limitation to this component in the following analysis. It has been shown by Boomsma et al. (2016) that these random errors are well predicted with the correlation statistics uncertainty quantification method.

To further assess the performance of the correlation statistics method to identify the random uncertainty components of the measured velocity field in towing tank applications, additionally a series of uniform flow measurements were performed. Furthermore these tests are performed to identify any bias introduced by the misalignment of the calibration plate. Since the laser is guided through the acrylic glass bottom of the model, the bottom has to be immersed in the water. To minimize the disturbance from the model on the flow, it is trimmed to 0° and its draft is changed to a minimum of 0.01 m. Afterwards the temporal statistics of the freestream flow are analyzed at a single point with a distance of 0.1 m from the ship bottom for carriage speeds from 3 m/s to 5 m/s. In all analyzed cases the laser pulse separation dt was chosen to yield a pixel displacement of approximately 10 pixels for the freestream velocity. Assuming still water before every measurement run, in the case of no obstruction in the flow, the disturbance of the flow is assumed to be negligible. Under the assumption that any measured velocity fluctuations are due to errors in the measurement system and the vector calculation procedure, the root mean square (RMS) of the estimated random uncertainties $RMS(U_u)$ should match the standard deviation of the measured velocities σ_u (Boomsma et al., 2016):

Table 1
Comparison of bias, errors and uncertainties from freestream tests for the different velocity components.

Vel. [m/s]	Comp.	Bias [px]	Error std. dev. [px]	Uncertainty RMS [px]
3	x	0.037	0.099	0.122
0	y	0.131	0.126	0.157
0	z	0.017	0.065	0.085
5	x	0.026	0.125	0.132
0	y	0.127	0.163	0.167
0	z	0.010	0.088	0.085

$$RMS(U_u) = \sqrt{\frac{\sum_{i=1}^{N} U_{u_i}^2}{N}} = \sqrt{\frac{\sum_{i=1}^{N} (u_i - \bar{u})^2}{N}} = \sigma_u \tag{7}$$

Here, U_{u_i} describes the standard uncertainty, obtained with the correlation statistics method. u_i describes the instantaneous velocity and $\bar{u}$ the temporal average of the velocity. Table 1 shows the uncertainty estimates and calculated errors for 3 m/s and 5 m/s freestream velocities. While the bias for the vertical velocity component is found to be negligible, the bias of the x and y velocity components indicate an initial rotation of the calibration target around the vertical axis of approximately 0.2°. For all velocity components, the RMS of the estimated uncertainty is slightly over predicted, compared to the standard deviation of the measured velocities. An explanation for this over prediction may be found by looking at the uncertainty quantification procedure, where next to random errors also small bias errors can be introduced for larger particle image sizes, where the PIV algorithm does not converge to a fixed value. While in both cases the water was considered to be at rest, the increasing fluctuations at a higher carriage velocity may be due to an increase of the structural vibrations.

Having reported an estimation of the uncertainty in the undisturbed flow, it has to be noted that the uncertainty can vary significantly in space, depending on the local characteristics of the flow. In the present case it is expected for the uncertainty to significantly increase in the boundary layer region due to the higher velocity gradient. As shown by van Doorne et al. (2004) in areas with no velocity gradient, the registration error is zero, but increases in regions with high velocity gradients, due to the mismatch of the back projected images. Especially at high speeds this component is considered to be the largest uncertainty component, due to the structural vibrations of the carriage. Furthermore the correlation noise is expected to increase towards the ship hull, due to the turbulent flow in the boundary layer. Fig. 5 shows an example of the RMS of the velocity field uncertainty contours calculated from 200 images. The model speed is 3 m/s and the interceptor height is 20 mm. A clear difference between the boundary layer region and the

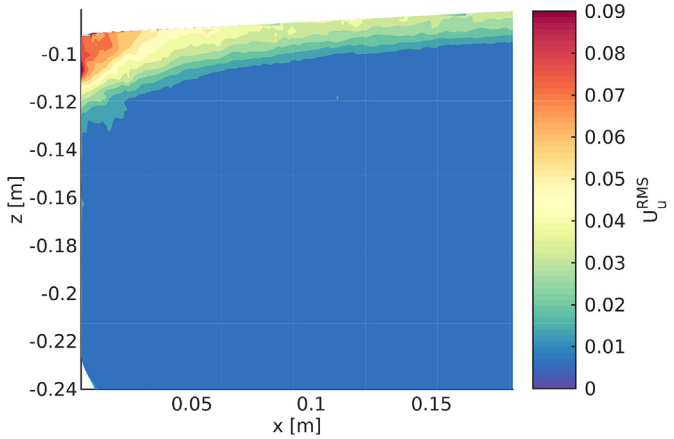

Fig. 5. Spatial variation of the RMS of the velocity field uncertainty at V_c = 3m/s with interceptor height h= 20 mm.

outer free-stream region can be seen. While values in the outer region are in compliance with the initial freestream reference runs, the uncertainty increases towards the boundary layer. Highest values are found in the stagnation region close to the interceptor with uncertainties up to 3% of the freestream velocity component.

4.2. Uncertainty propagation

As the main uncertainty components are of random nature, their magnitude scales with the number of samples N when calculating the uncertainty of the time averaged velocity field components. Following Sciacchitano and Wieneke (2016) the uncertainty of the mean velocity $U_{\bar{u}}$ can be calculated as:

$$U_{\bar{u}} = \frac{\sigma_u}{\sqrt{N}} \tag{8}$$

However, the velocity standard deviation σ_u contains the true velocity fluctuations, as well as the measurement errors. Having quantified the spatial uncertainty distributions for every time step with the correlation statistics method, instead of using Equation (8) the uncertainties from every time step are propagated towards the uncertainty of the mean velocity $U_{\bar{u}}$, using the uncertainties of the instantaneous velocities U_{u_i}:

$$U_{\bar{u}} = \frac{\sqrt{\sum_{i=1}^{N} U_{u_i}^2}}{N} \tag{9}$$

Using the derived formulas from Sciacchitano and Wieneke (2016) also the uncertainty of the Reynolds stresses can be determined. As the uncertainties of the mean velocity field are small compared to the velocity fluctuations, the uncertainty of the normal stresses equals the uncertainty of the variance:

$$U_{R_{uu}} = \sigma_u^2 \cdot \sqrt{2/(N-1)} \tag{10}$$

The uncertainty of the Reynolds shear stress can be calculated with the covariance uncertainty equation, which, under the assumption of a zero correlation coefficient, is:

$$U_{R_{uv}} = \sigma_u \sigma_v / \sqrt{N-1} \tag{11}$$

Due to the non-linearity of the Poisson pressure equation (3), according to ISO (2009), a Monte Carlo approach is chosen to propagate the assessed uncertainty components of the mean velocity and Reynolds stresses to the time-averaged pressure field $\bar{p}$. Compared to the linear uncertainty propagation, described according to ISO (2008), this method gives a generally improved estimate of the output quantity $\bar{p}$. As found by Azijli et al. (2016), a linear uncertainty propagation of the measured components towards the pressure field leads to an underestimation of pressure uncertainty by about 30% compared to results from Monte Carlo simulations. Under the assumption of the measured input variables to be Gaussian distributed, simulations with 10.000 realizations are done to evaluate the uncertainty of the reconstructed pressure field. The Monte Carlo simulations were performed within the OpenFOAM package, using the GaussNormal member function of the Random class to generate variations of the input variables. The final expanded uncertainty $U_{\bar{p},95}$ is then calculated by multiplying the resulting standard uncertainty with a coverage factor of 2 for a confidence interval of 95%. As seen in Fig. 6 the expanded uncertainty in the freestream region is below 0.5% of the maximum pressure and increases towards the boundary layer. Starting from approximately x/h = 1 the uncertainty increases significantly to up to 6.5% of the peak pressure right in front of the interceptor.

Knowing the discrete uncertainty distribution of the pressure field on the ship hull, the uncertainty of the sectional lift can be estimated as:

$$U_l = \sqrt{\sum_{i=1}^{N} U_{\bar{p}_i}^2 \, ds_i^2} \tag{12}$$

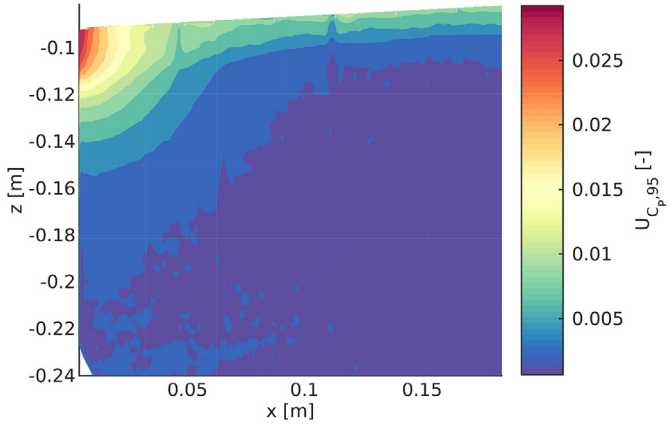

Fig. 6. Pressure uncertainty map from propagated uncertainties at 95% confidence level at V_c = 3m/s with interceptor height h= 20 mm.

5. Numerical simulations

For a comparison of the obtained PIV results with numerical results, CFD simulations of the performed towing tank tests are made with the open source code OpenFOAM 5.0. The incompressible unsteady Reynolds-Averaged Navier-Stokes equations are solved with the interFoam solver, where the Volume of Fluid (VOF) approach is applied to capture the two-phase interface. The governing equations are discretized with second-order central differencing schemes and a two-equation k-omega-SST model is used for modelling the turbulence. As the ship model is symmetric, only one half of the ship is meshed to reduce the number of cells. The numerical grid is generated with the hexahedral mesher snappyHexMesh, which is modified to fit the needs for meshing of marine applications and allow for higher aspect ratio cells in the free surface region. After calculating an initial solution with a coarse grid, the grid is further refined in the free-surface region and in front of the interceptor. An example of the final mesh in the free surface region is depicted in Fig. 7 including the dimensions of the domain. While the cross-section of the domain was chosen to fit the TU Delft towing tank dimensions, the outlet position of the domain was chosen according to the ITTC guidelines (ITTC, 2011) to prevent wave reflection. Also depicted in Fig. 7 is the refined region in front of the interceptor with the prismatic boundary layers inserted on the ship hull.

The total mesh consisted of approximately 3.5 million cells with a dimensionless wall distance y^+ of 1 on the ship hull. To analyze the accuracy of the simulations the lift, generated by the interceptor in the aft section of the model, is compared the results of segmented model tests performed by Rijkens et al. (2013). Fig. 8 shows the comparison of the generated lift force on the aft segment of the ship hull for different speeds and interceptor intrusion heights. The lift force generated by the hull without interceptor is subtracted from the results. The numerical results are found to be in good agreement with the experimental results. Especially for interceptor heights up to 15 mm the comparison error is below 2%. Interestingly at interceptor heights of 20 mm the CFD results systematically under predict the measured lift force. The maximum comparison error here is approximately 6%.

6. Discussion and comparison of experimental and numerical results

6.1. 2d results

The flow field in front of the interceptor is recorded in the center plane of the ship model while systematically varying of intruder height and ship speed. While the ship hull is considered to be symmetrical, the flow in the center plane can be considered to be two dimensional with no out of plane velocity. As shown by Brizzolara (2003), already small

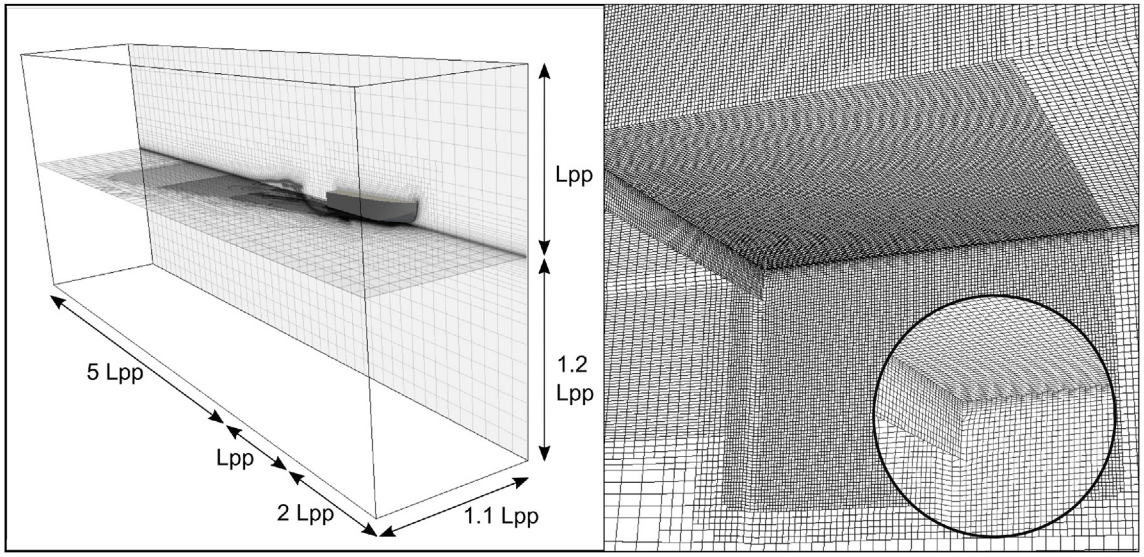

Fig. 7. Computational domain with main dimensions (left); Refined mesh in front of the interceptor with detail view of the boundary layer mesh (right).

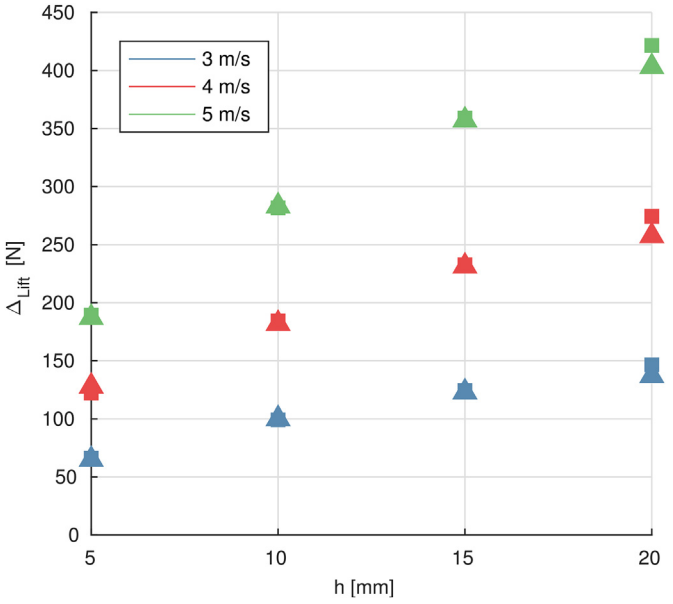

Fig. 8. Comparison of lift forces from numerical simulations (■) and segmented model tests (▲) acting on the aft model section.

changes in the boundary layer shape can significantly change the pressure distribution in front of the interceptor. Following from this, it has to be made sure that the simulated flow field close to the ship hull is in good agreement with the experimental conditions before comparing simulated and reconstructed pressure fields. Fig. 9 gives an insight into the flow in front of the interceptor close to the ship hull. The mean velocity and pressure profiles in the center plane of the model are plotted for different stations in front of the transom. Results are presented for an interceptor intrusion height of 20 mm. Measured velocities and reconstructed pressures are compared to results from the performed CFD calculations to judge the quality of the near wall resolution. The velocity magnitude is made dimensionless with the free-stream velocity. Wall distance and longitudinal distance from the transom are expressed relative to the interceptor height h. Affected by the adverse pressure gradient which is generated by the interceptor, the flow in the boundary layer is decelerated towards the transom. Measured and simulated velocity and pressure profiles are in good agreement with each other. While Jacobi et al. (2016) found larger differences in the near wall velocity field, a grid refinement in wall normal direction with resulting $y^+ = 1$ could improve the agreement of the simulation results with the velocity profiles found from PIV measurements. As expected, the good agreement of the velocity field in the boundary layer also leads to a good agreement of the reconstructed and simulated pressures.

Contour plots of the reconstructed pressure field in front of the interceptor in the center plane of the model are depicted in Fig. 10, where they are compared to the simulation results. Pressure fields are shown for 10 mm and 20 mm interceptor intrusion heights. While the contours of the reconstructed fields are affected by noise, there is still a good agreement with the simulations. Largest differences can be found close to the interceptor in the stagnation region where both reconstructed results give a higher maximum pressure compared to the simulations. However, both simulations and measurements clearly show an increase of the peak pressure in front of the interceptor with increasing blade height.

To further analyze the dependency of the pressure distribution on the ship hull on interceptor height, the pressure distribution on the hull is plotted in Fig. 11 for interceptor heights increasing from 0 to 20 mm in steps of 5 mm at constant model speed. As shown in Fig. 9, the velocity field and thus the pressure field is well resolved close to the wall. This justifies the assumption that the reconstructed pressure in the upper most cells represents the surface pressure on the ship hull under the assumption of a zero pressure gradient in wall normal direction. While the lines represent the CFD results, the dots represent the reconstructed pressures. As the original resolution of the PIV vector grid resulted in a total of approximately 135 measurement points over length of the measurement section on the ship hull, for the sake of clarity only every fourth measurement point is plotted. In all conditions the flow is smoothly separating from the transom, leaving the transom dry. Resulting from this, without any interceptor the pressure drops to atmospheric pressure towards the transom due to the presence of the free surface, leading to a negative dynamic pressure at the transom. Due to the stagnation region in front of the interceptor, this pressure becomes positive, and is increasing with interceptor height. Also the point of separation shifts further forward, resulting in an increasing region of constant pressure right in front of the interceptor. Both, results from measurements and simulation are in good agreement with each other, with largest differences in the region of the pressure peak. However, the difference of the peak pressures still lies within the uncertainty band of the PIV results, which was estimated to be approximately 6% of the peak pressure value in this region.

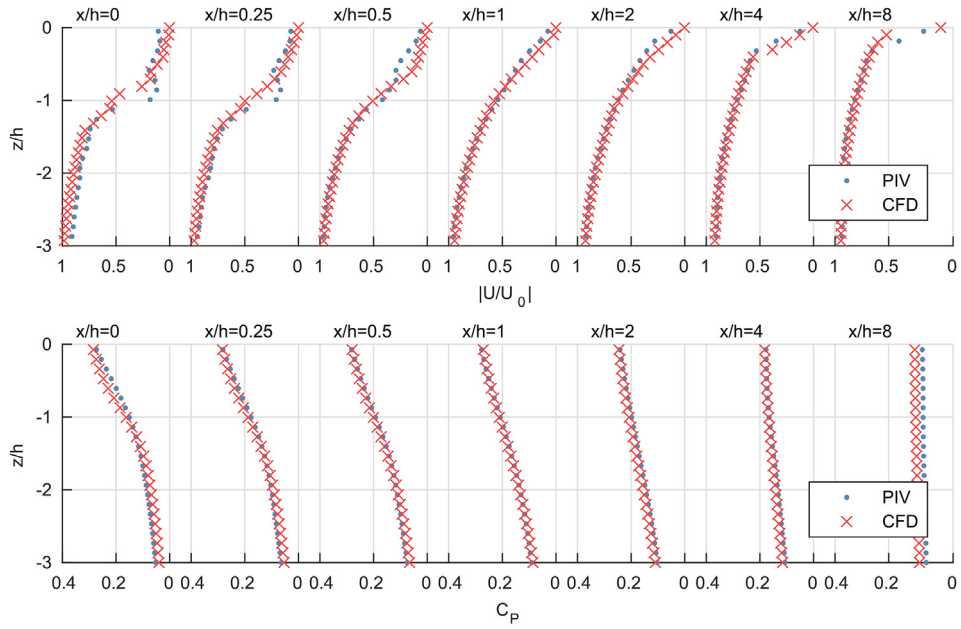

Fig. 9. Velocity profiles normal to the ship hull at different stations in front of interceptor (top); Corresponding pressure profiles normal to the ship hull at different stations in front of the interceptor (bottom).

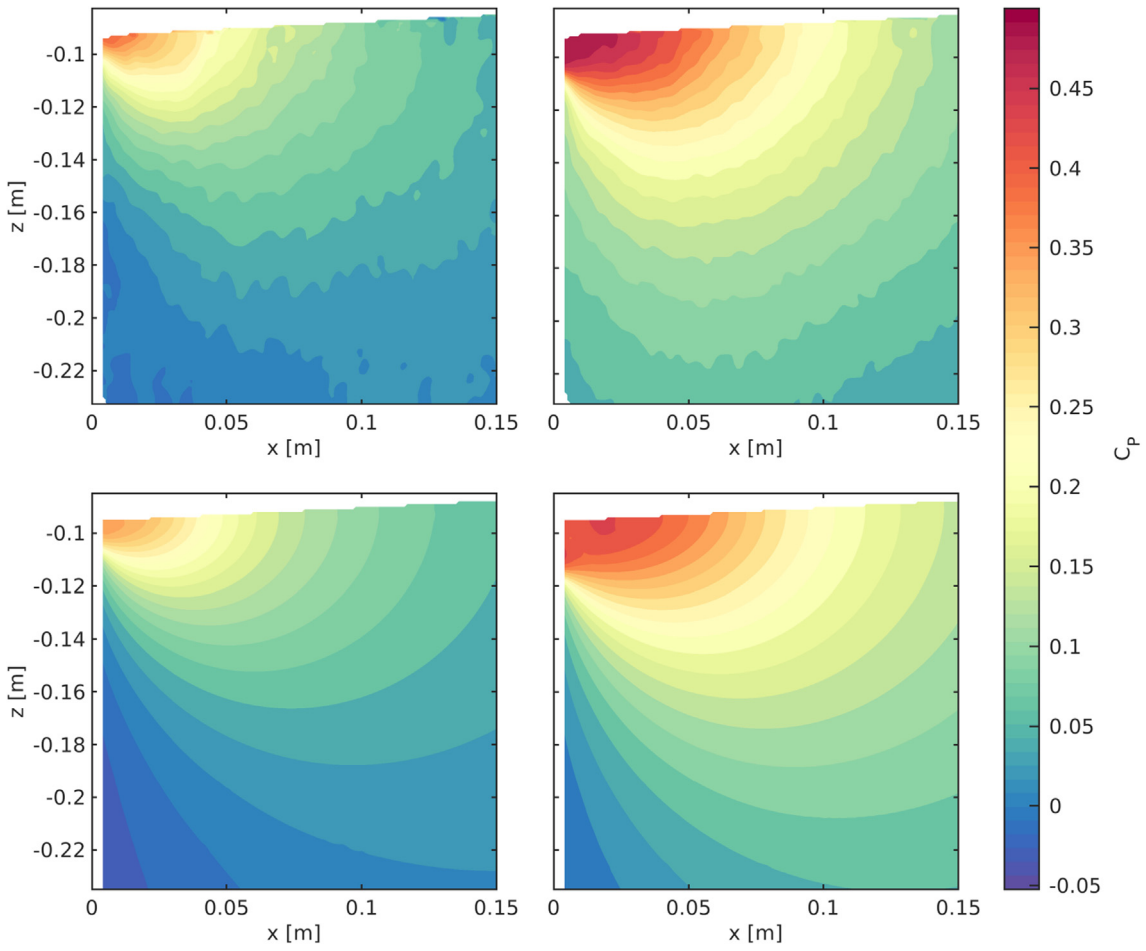

Fig. 10. Comparison of reconstructed (top) and simulated (bottom) pressure contours for interceptor heights of 10 mm (left) and 20 mm (right) at 3 m/s.

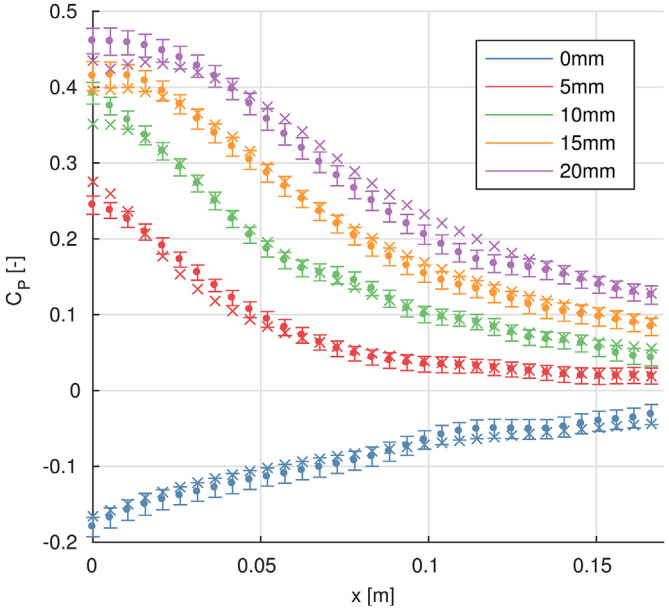

Fig. 11. Influence of the interceptor height on the pressure distribution on the ship hull in the center plane of the model – comparison of reconstructed pressures (•), including their extended uncertainty bounds, with results from numerical simulations (×).

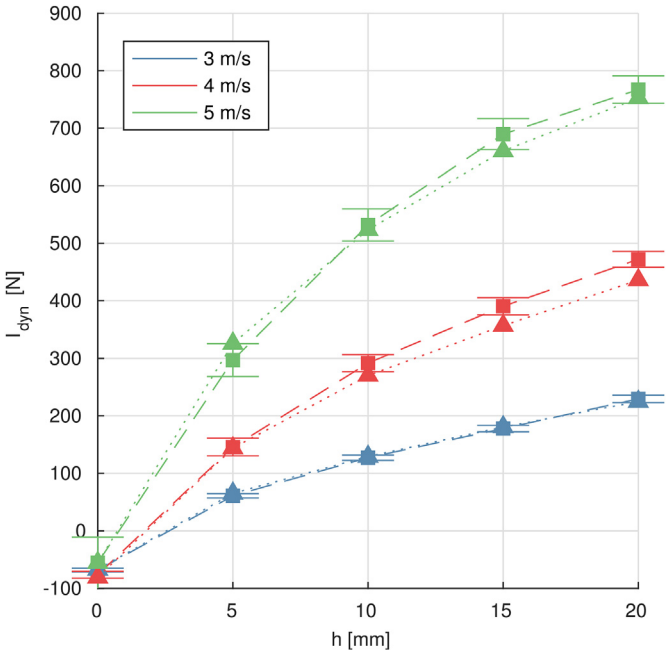

Fig. 12. 2d lift force dependence on interceptor height (h) and model speed – comparison of reconstructed lift force (■), including extended uncertainty bounds, with results from numerical simulations (▲).

The reconstructed 2d pressure fields in the center plane of the ship hull were integrated to yield the total dynamic lift force component in the aft region of the ship disregarding any 3d effects. Fig. 12 shows the lift force for all analyzed speeds and interceptor heights per unit ship width and compares experimental results and their calculated uncertainty with results from CFD simulations. The uncertainties of the integral forces were found from integrating the uncertainties of the single measurement points. While for 3 m/s experimental results are in good agreement with simulations, the integrated values at 4 and 5 m/s are slightly over predicted for most analyzed conditions with maximum differences of approximately 8 percent. As the laser pulse separation has been initially chosen to yield a constant pixel displacement in the freestream for all tested velocities, the actual uncertainty values increase proportionally with carriage velocity. This trend is also propagated to the integral forces.

6.2. 3d results

For selected conditions at 3 and 4 m/s the measurement planes were shifted stepwise towards the side of the model to reconstruct a volumetric velocity field from a total of 14 measurement planes and analyze the three-dimensionality of the flow around the interceptor. Fig. 13 shows contour plots of the three velocity components and reconstructed pressures at 3 transverse positions from a selected run with an interceptor height of 20 mm at a speed of 3 m/s. At y = 0, in the center plane of the ship model, the mean flow is purely two-dimensional. While the out of plane component is close to zero in the whole field of view, the in plane components show a deceleration of the flow towards the interceptor in x direction and an acceleration in z direction. As seen from the contour plots at y = 0.75b/2 and b/2, with b being the ship width, the out of plane component steadily increases towards the side of the model, while the downward component decreases. With the increasing out of plane component towards the side of the interceptor blade, the high pressure region in front of the interceptor significantly reduces in size.

The reconstructed volumetric pressure field has been extrapolated to the ship hull to further analyze the three dimensional effects of the flow on the surface pressure distribution. Results presented in Fig. 14 show the reconstructed pressure coefficient on the ship hull for interceptor heights of 10 and 20 mm at 3 m/s model speed on an area of 180 × 190 mm^2. Further, measurement results are compared to pressure distributions which were obtained from CFD simulations. As already seen in Fig. 13, due to the increased transverse flow component in front of the interceptor, the pressure reduces towards the side of the interceptor blade. While there is a good agreement between results from CFD and PIV measurements, largest deviations can be found in the peak pressure region. As already seen from the two dimensional results, the reconstructed peak pressure form the PIV measurements is slightly higher compared to the CFD results.

An integration of the surface pressure along the ships longitudinal direction at different transverse sections quantifies the hydrodynamic lift reduction towards the side of the interceptor due to the three dimensionality of the flow. Fig. 15 shows the sectional lift coefficient and its uncertainty from all 14 measurement planes and compares them to the numerical results. Results from experiments and simulations both clearly show a reduction of lift towards the side of the interceptor and are in good agreement with each other for all analyzed velocities and interceptor heights. Due to the over prediction of the pressure peak in the center planes of the ship, here the total dynamic lift is also over predicted by the pressure reconstruction from PIV results. However, an integration of the sectional loads over the width of the ship leads to maximum differences of approximately 3% of the hydrodynamic lift between experimental and numerical results. General conclusions about the lift reduction due to three dimensional effects and its dependency on interceptor height and speed cannot be drawn from these results, as the measurement area was too small and no volumetric field has been reconstructed for runs without interceptor.

7. Conclusion

The present study has been conducted to evaluate an alternative means of measuring the surface pressure distribution on a ship model during towing tank tests while studying the characteristics of the flow around an interceptor. For this purpose an underwater stereo PIV system has been utilized to measure the mean velocity field close to the ship. These results eventually have been used together with the Poisson

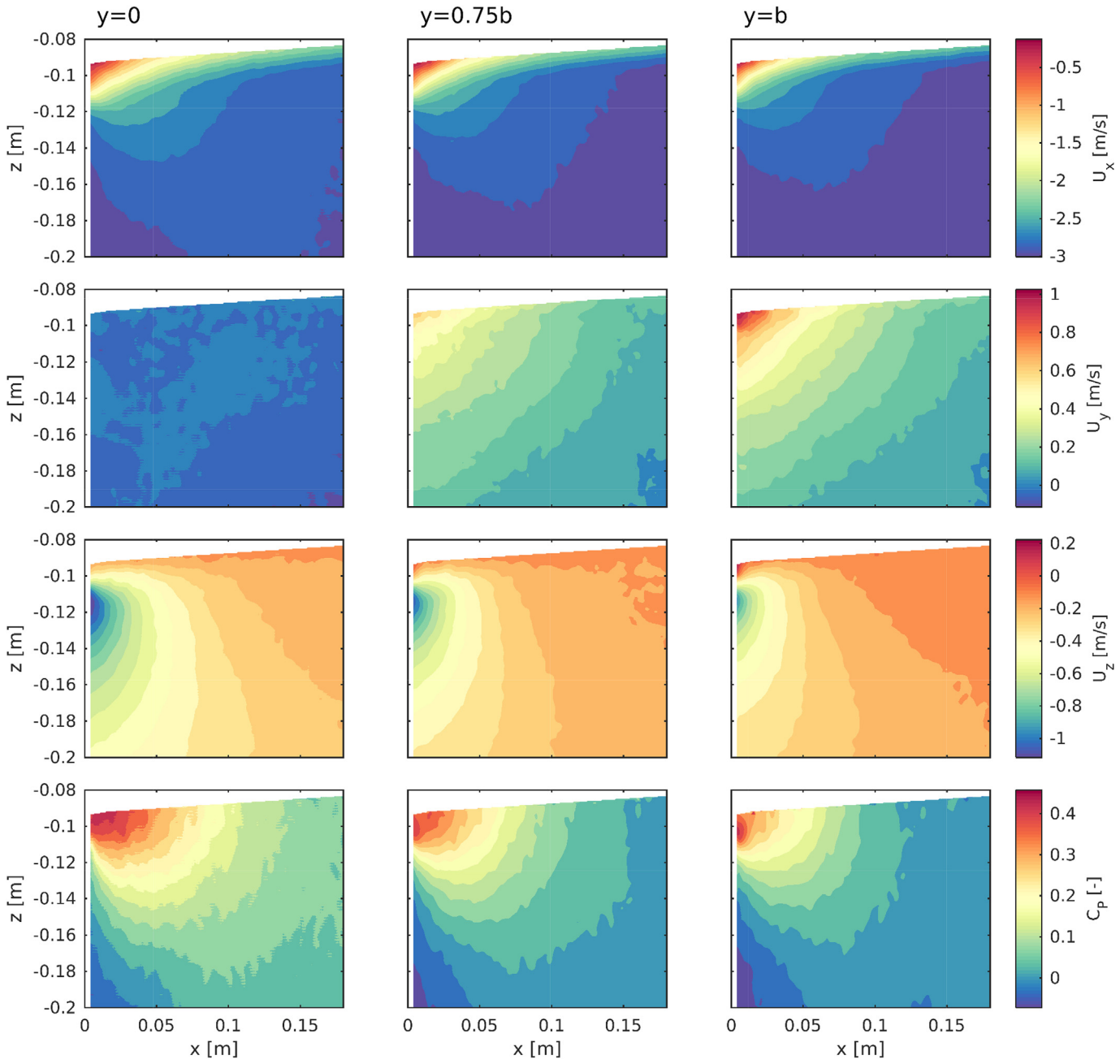

Fig. 13. Velocity components at different transverse positions with reconstructed pressure fields.

pressure equation to reconstruct the average pressure field in the flow field as well as on the ship model. While a broader range of conditions was analyzed with single plane PIV measurements in the center plane of the model, for selected conditions also a volumetric flow field, spanning the whole width of the transom, could be reconstructed from multi-plane stereo PIV measurements. When comparing experimental results with those from simulations, often the question arises if the experimental conditions have been accurately modelled in the numerical simulations. Especially in the case of the flow in front of an interceptor, the pressure distribution is very sensitive to differences in boundary layer characteristics (Brizzolara, 2003). By comparing the measured velocity field in front of the interceptor with results from simulations it was made sure that the experimental conditions were accurately reproduced within the numerical simulations. The following analysis of the dynamic pressure fields for a range of interceptor heights and model speeds showed that the pressure distribution in the flow field, as well as the extrapolated pressures on the ship hull are in good agreement with each other. With performing multiplane stereo PIV measurements an alternative technique is proposed to measure the average dynamic pressure distribution on a whole segment of a ship model. In case of the present study the 3d effects of an interceptor with a finite span on the pressure distribution on the ship hull were successfully captured. However, for a systematic study of the effect of the three dimensionality of the flow more configurations have to be analyzed. To judge the accuracy of the reconstructed pressures, the correlation statistics method of Wieneke (2015) has been applied to quantify the random uncertainty component of the recorded velocity field which was afterwards propagated towards the pressure field with Monte Carlo simulations. The resulting uncertainty maps of velocity and pressure fields showed large local variations with a steep increase of uncertainty values in the boundary layer of the ship model emphasizing the need for such a method and not only rely on freestream measurements. However, the

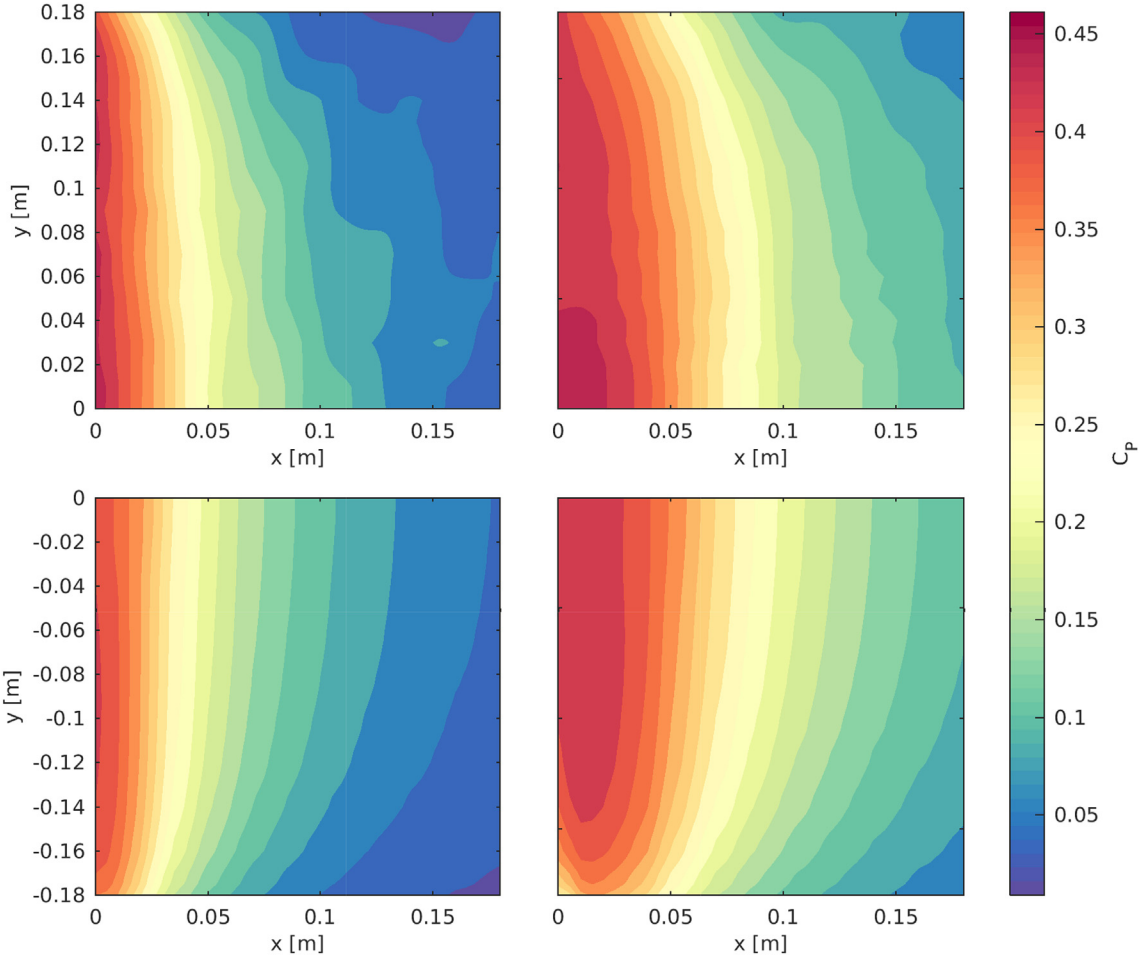

Fig. 14. Comparision of reconstructed pressure fields on the ship model (top) with results from CFD simulations (bottom) at 3 m/s and interceptor heights of 10 mm (left) and 20 mm (right).

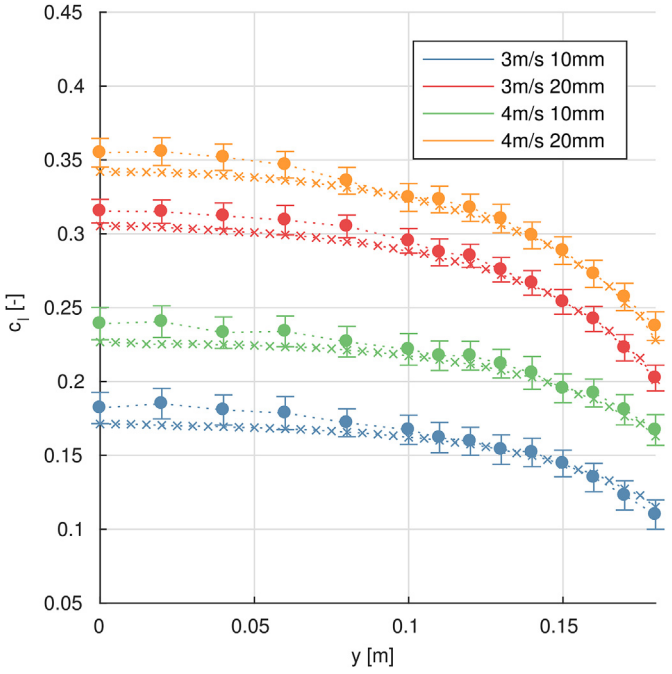

Fig. 15. Lift coefficients for varying speeds and interceptor heights at different transverse sections – comparison of reconstructed lift force (•), including extended uncertainty bounds, with results from numerical simulations (×).

combination with freestream measurements is advised as a good measure to identify and correct for any systematic errors, such as calibration target misalignment.

The presented technique has proven to be an interesting fully non-intrusive alternative to the existing methods which are currently used in towing tank tests. Especially when only the dynamic pressure distribution is of interest, this technique offers several advantages. However due to spatial as well as temporal limitations it does not make segmented model test or test with arrays of pressure transducers obsolete. While the current study has shown the potential of the method for towing tank applications, further effort has to be put into validation of the method and comparisons with pressure gauge arrays have to be made. As the focus has been on time averaged measurements only, also the limitations and accuracy of performing time resolved pressure PIV measurements in towing tanks need to be further investigated.

References

Albrecht, T., del Campo, V., Weier, T., Gerbeth, G., 2012. Comparison of PIV-based methods for airfoil loads evaluation. In: Symposium on Applications of Laser Techniques to Fluid Mechanics, pp. 9–12 July 2012.

Azijli, I., Sciacchitano, A., Ragni, D., Palha, A., Dwight, R.P., 2016. A posteriori uncertainty quantification of PIV-based pressure data. Exp. Fluid 57 (5), 1–15.

Boomsma, A., Bhattacharya, S., Troolin, D., Pothos, S., Vlachos, P., 2016. A comparative experimental evaluation of uncertainty estimation methods for two-component PIV. Meas. Sci. Technol. 27 (9).

Brizzolara, S., 2003. Hydrodynamic analysis of interceptors with Cfd methods. In: 7th Int. Conf. Fast Sea Transp, pp. 49–56.

Choi, B., 2018. Influence of Bow-Wave Breaking on the Added Resistance of Fast Ships (Ph.D. thesis). .

De Jong, P., Keuning, J.A., 2006. 6-DOF forced oscillation tests for the evaluation of

nonlinearities in the superposition of ship motions. Int. Shipbuild. Prog. 53, 123–143.
ISO, 2008. ISO/IEC Guide 98-3:2008(E) Uncertainty of Measurement - Part 3: Guide to the Expression of Uncertainty in Measurement (GUM:1995).
ISO, 2009. ISO/IEC Guide 98-3/SI/AC1:2009(E) Uncertainty of Measurement - Part 3: Guide to the Expression of Uncertainty in Measurement (GUM:1995), Supplement 1: Propagation of Distributions Using a Monte Carlo Method, Technical Corrigendum 1.
ITTC, 2011. Practical Guidelines for Ship CFD Applications.
Jacobi, G., Thill, C.H., Huismans, R.H.M., 2016. The application of particle image velocimetry for the analysis of high-speed craft hydrodynamics. In: Int. Conf. Hydrodyn.
Keuning, J.A., 1994. Nonlinear Behaviour of Fast Monohulls in Head Waves (Ph.D. thesis). .
Mansoori, M., Fernandes, A.C., 2015. Hydrodynamics of the interceptor on a 2-D flat plate by CFD and experiments. J. Hydrodyn. 27 (6), 919–933.
McLachlan, B.G., Bell, J.H., 1995. Pressure-sensitive paint in aerodynamic testing. Exp. Therm. Fluid Sci. 10 (4), 470–485.
Molini, A., Brizzolara, S., 2005. Hydrodynamics of interceptors: a fundamental study. In: Int. Conf. Mar. Res. Transp. Naples.
Nila, A., Vanlanduit, S., Vepa, S., Van Paepegem, W., 2013. A PIV-based method for estimating slamming loads during water entry of rigid bodies. Meas. Sci. Technol. 24 (4).
Pearce, B., Brandner, P., 2014. Inviscid cavity flow over a wall-mounted fence. Ocean Eng. 80, 13–24.
Ragni, D., Van Oudheusden, B.W., Scarano, F., 2012. 3D pressure imaging of an aircraft propeller blade-tip flow by phase-locked stereoscopic PIV. Exp. Fluid 52 (2), 463–477.
Rijkens, A.A.K., Cleijsen, H.M.A., Keuning, J.A., 2013. On the hydrodynamic performance of an improved motion control device for fast ships. In: 12th Int. Conf. Fast Sea Transp.
Sakaue, H., Ozaki, T., Ishikawa, H., 2009. Global oxygen detection in water using luminescent probe on anodized aluminum. Sensors 9 (6), 4151–4163.
Sciacchitano, A., Wieneke, B., 2016. PIV uncertainty propagation. Meas. Sci. Technol. 27 (8).
Tagliabue, A., Scharnowski, S., Kähler, C.J., 2017. Surface pressure determination: a comparison between PIV-based methods and PSP measurements. J. Vis. 20 (3), 581–590.
van Doorne, C., Westerweel, J., Nieuwstadt, F., 2004. Measurement uncertainty of stereoscopic-PIV for flow with large out-of-plane motion. In: Part. Image Velocim. Recent Improv. Springer, Berlin, Heidelberg, pp. 213–227.
Van Oudheusden, B.W., 2013. PIV-based pressure measurement. Meas. Sci. Technol. 24 (3).
Villa, D., Brizzolara, S., 2009. A systematic CFD analysis of flaps/interceptors hydrodynamic performance. In: 10th Int. Conf. Fast Sea Transp, pp. 1023–1038.
Wieneke, B., 2005. Stereo-PIV using self-calibration on particle images. Exp. Fluid 39 (2), 267–280.
Wieneke, B., 2015. PIV uncertainty quantification from correlation statistics. Meas. Sci. Technol. 26 (7).